processes

MDPI

Article

Optimization of Ternary Activator for Enhancing Mechanical Properties of Carbonized Cementitious Material Based on Circulating Fluidized Bed Fly Ash

Nuo Xu, Suxia Ma *, Nana Wang, Yuchuan Feng, Yunqi Liu, Ke Ren and Shanshui Bai

Shanxi Province Key Laboratory of Clean & High Efficient Combustion and Utilization of Circulating Fluidized Bed, Taiyuan University of Technology, 79 Yingze West Street, Taiyuan 030024, China; xunuo0322@link.tyut.edu.cn (N.X.); wangnana01@tyut.edu.cn (N.W.); fengyuchuan@tyut.edu.cn (Y.F.); liuyunqi2021@163.com (Y.L.); renke0449@link.tyut.edu.cn (K.R.); baishanshui0332@link.tyut.edu.cn (S.B.)

* Correspondence: masuxia@tyut.edu.cn

Abstract: In this study, circulating fluidized bed fly ash (CFBFA) non-sintered ceramsite was innovatively developed. The CFBFA was addressed by adding ternary activator (including cement, hydrated lime, and gypsum) to prepare ceramsite. In the curing process, the use of power plant flue gas for curing not only captured greenhouse gas CO_2, but also enhanced the compressive strength of the ceramsite. The compressive strength of the composite gravels prepared by the CFBFA was modeled using a novel approach that employed the response surface methodology (RSM) and artificial neural network (ANN) coupled with genetic algorithm (GA). Box–Behnken design (BBD)-RSM method was used for the independent variables of cement content, hydrated lime content, and gypsum content. The resulting quadratic polynomial model had an R^2 value of 0.9820 and RMSE of 0.21. The BP-ANN with a structure of 3-10-1 performed the best and showed better prediction of the response than the BBD-RSM model, with an R^2 value of 0.9932 and RMSE of 0.19. The process parameters were optimized using RSM optimization tools and GA. Validation experiments showed that the GA-ANN prediction results were more accurate than the BBD-RSM results.

Keywords: ternary activator; Box–Behnken design; response surface methodology; artificial neural network; genetic algorithm

check for updates

Citation: Xu, N.; Ma, S.; Wang, N.; Feng, Y.; Liu, Y.; Ren, K.; Bai, S. Optimization of Ternary Activator for Enhancing Mechanical Properties of Carbonized Cementitious Material Based on Circulating Fluidized Bed Fly Ash. *Processes* **2024**, *12*, 289. https://doi.org/10.3390/pr12020289

Academic Editor: Carlos Sierra Fernández

Received: 29 December 2023
Revised: 20 January 2024
Accepted: 23 January 2024
Published: 29 January 2024

1. Introduction

Circulating fluidized bed (CFB) combustion technology has received significant attention in the thermal power sector due to its high efficiency [1,2], low pollution, clean production, and widespread availability [3]. CFB fly ash (CFBFA) is a by-product of CFB. The large-scale utilization of CFBFA has been inadequate. Stacking CFBFA is still the main disposal method at present. However, stacking CFBFA causes a series environment issue. The preparation of CFBFA recycled concrete aggregate is an effective method.

CFBFA has active volcanic ash properties and self-hardening characteristics [4–6]. It contains various elements such as Al_2O_3, SiO_2, CaO, Fe_2O_3, and MgO. These properties make CFBFA suitable for various construction materials. For example, it can be used in the production of clay bricks [7], recycled concrete aggregate, ceramic membrane [8], and concrete. Ceramsite can be used as recycled concrete aggregate. The high temperature sintering method and the non-sintering method are two methods to produce ceramsite using fly ash. Qin et al. [9] utilized ceramsite from coal fly ash to produce lightweight concrete instead of natural sand and gravel aggregates. Jia et al. [10] utilized a high-temperature sintering method to produce CFB fly ash ceramsite, resulting in enhanced stability of the ceramsite. The high-temperature sintering method typically necessitates temperatures exceeding 1000 °C to effectively solidify ceramsites. Sulfur release and high energy consumption are the problems of ceramsite prepared by high temperature sintering.

CFBFA ceramsite has been prepared by sintering method, but no low energy consumption method has been proposed. In comparison to sintered ceramsite, non-sintered ceramsite offers several advantages including low cost, a simple production method, lightweight construction, high strength, and environmental friendliness [11]. While most of the current research focuses on the high-temperature preparation of sintered ceramsites, there is relatively less emphasis on studying the production and performance of non-sintered ceramsites. This study aims to develop a novel type of non-sintered CFBFA ceramsites. In this study, the novel ceramsite is called composite gravels. The no-sintered ceramsite is to use the gelling property of the fly ash for bonding. The stronger the activity of fly ash, the stronger its cementitious ability. The activity of CFBFA is cruel to the compressive strength of composite gravels. CFBFA exhibits self-cementitious activity, resulting in the hardened paste acquiring a certain level of compressive strength [12]. Research has shown that the activity of fly ash can be enhanced by incorporating additives such as cement [13], hydrated lime [14], and gypsum [15]. Illikainen et al. [16] observed that minerals like C_3A and C_2S present in cement react with fly ash to form ettringite and C-S-H gels. However, cement-activated fly ash is susceptible to degradation by sulfate found in fly ash [17]. Iribarne et al. [18] introduced hydrated lime to fly ash to enhance the activity of volcanic ash within it. Additionally, Moghal [19] et al. incorporated gypsum into fly ash, which further increased the pozzolanic activity of the fly ash.

The properties of composite gravels are primarily determined by the activator contents. Given the intricate nature of the combined influences of multiple factors, it is essential to establish a suitable data analysis model to achieve effective performance optimization. Response surface methodology (RSM) and artificial neural network (ANN) have been extensively utilized to enhance the efficiency of data optimization [20,21]. RSM has found wide application in various fields, including process optimization and control. In the context of building materials, researchers have employed RSM to optimize the mechanical strength [22]. On the other hand, the ANN approach serves as a robust mathematical tool capable of modeling diverse behaviors, including complex non-linear relationships [23]. The application of ANN has been extensively conducted in various fields of construction engineering, including non-destructive testing technology [24], predicting the compressive strength of concrete technology [24], time series forecasting the production activity technique [25], etc.

The utilization of carbonization curing emerges as a pivotal strategy in enhancing the performance of cementitious materials, concurrently contributing to carbon neutrality by sequestering CO_2 [26]. Carbonization curing can improve the early compressive strength of the cementitious material rapidly [27]. The application of CO_2 curing technology demonstrates superior early compressive strength and heightened impermeability [28]. This transformative process is often accompanied by the precipitation of calcium carbonate ($CaCO_3$) within the pores of cementitious materials, culminating in amplified refinement of microstructure and mechanical strength [29]. Monkman et al. [30] also found that during carbonization curing, $CaCO_3$ forms within the cementitious material, filling the pore structure and augmenting the solid volume. This phenomenon not only optimizes microstructure but also contributes to increased mechanical strength. In addition, Zhan et al. [31] discovered that the effectiveness of carbonization curing is intricately linked to various factors such as water content, gas pressure, and curing time of the cementitious material. The interplay of these parameters significantly influences the progress and outcomes of the carbonization curing process.

Previous studies have not clearly explained the coupling activation mechanism of the three activators. The action mechanism of these three activators involves many chemical reactions, and the action mechanism is complex. At present, there are few studies on the combined effects of these three activators. The understanding of this coupling activation remains limited in the existing literature.

In this study, power plant flue gas curing was innovatively used. High temperature and high pressure carbonization curing process has high energy consumption and complex process. In this paper, the coal flue gas of the power plant is used, which has 15% CO_2. The use of flue gas in the curing process can not only capture greenhouse gas CO_2, but also enhance the compressive strength of the composite gravels. In addition, f-CaO in CFBFA will expand when the composite gravel meets water in actual use, resulting in volume instability. The carbonization curing can consume f-CaO in CFBFA and prevent the composite gravels from volume expansion and cracking. In this paper, cement, hydrated lime, and gypsum were used to prepare composite gravels. The Box–Behnken design (BBD)-RSM and the genetic algorithm (GA)-ANN were used to model and optimize the compressive strength of composite gravel. By considering cement, hydrated lime, and gypsum as independent variables and compressive strength of composite gravels as the dependent variable, the RSM test estimates the effects of the independent variables on the response. The interaction effects can be visually illustrated through response surface plots of the variables. Finally, the predictive ability and modeling efficiency of the two models are compared and validated. To further understand the intrinsic mechanism of carbonated cementitious materials prepared from CFBFA, X-ray diffraction (XRD) and Fourier transform infrared spectroscopy (FTIR) are utilized to analyze reaction products. High-temperature weight loss is analyzed through thermogravimetric analysis (TG-DTG), and microstructure is observed via scanning electron microscopy (SEM).

2. Experiment

2.1. Materials

The CFBFA used in this study was provided by Shanxi Jinneng Datuhe Thermal Power Co., Ltd., Lvliang, China. The gypsum and hydrated lime used in this study were purchased from Shanghai Aladdin Biochemical Technology Co., Ltd., Shanghai, China. Portland cement (P.O. 42.5) was manufactured by Jiuqi Building Materials Co., Ltd., Zibo, China. The chemical compositions of the mineral admixtures utilized in this study are provided in Table 1. Particle size distributions of CFBFA, cement, and hydrated lime were measured by a laser particle size tester (BT-9300HT, Bettersize was purchased from Dandong Baxter Instrument Co., Ltd., Dandong, China). Figure 1 shows the particle size distribution curves of CFBFA, cement, gypsum, and hydrated lime. According to the results, the specific surface area of gypsum, CFBFA, cement, and hydrated lime were 84.95 m^2/kg, 333.6 m^2/kg, 213.0 m^2/kg, 974.5 m^2/kg and the median diameter of gypsum, CFBFA, cement, and hydrated lime were 49.66 μm, 16.98 μm, 21.89 μm, and 9.663 μm, respectively.

Table 1. Chemical composition of CFBFA, cement, hydrated lime, and gypsum./Wt%.

Material	SO_3	CaO	SiO_2	Al_2O_3	Fe_2O_3	MgO
CFBFA	3.967	5.762	40.886	34.704	8.053	2.567
Cement	4.029	53.678	21.245	7.298	4.591	6.037
Hydrated Lime	0.647	93.886	0.928	0.956	-	2.511
Gypsum	51.549	43.205	-	0.794	-	3.925

The raw materials, including CFBFA, Portland cement (P.O. 42.5), hydrated lime, and gypsum, were precisely weighed and proportioned before being introduced into a mixer. The materials were blended for five minutes and then transferred to a ball mill where they were subjected to ten minutes of milling. Subsequently, the mixture was processed in a rolling granulator for granulation. Throughout the process, the water-solid ratio was controlled to maintain a value of 0.33. All samples were cured at 80 °C, 0.4 MPa of simulated flue gas curing in a high-pressure reactor for one hour. The simulated flue gas consists of 15% carbon dioxide and 85% nitrogen. At last, the CFBFA composite gravels were put into the curing room for 28 days. The temperature control value of the curing room was 20.0 °C ± 1.0 °C, and the humidity control value was 95% ± 1.5%. The prepared CFBFA composite gravels have a diameter of about 10 mm.

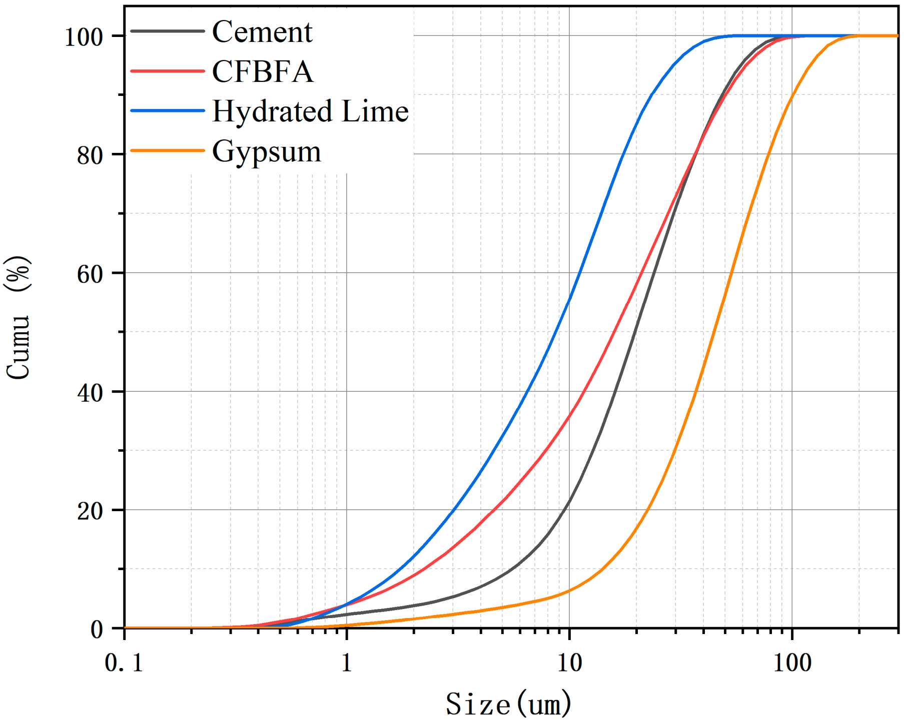

Figure 1. Particle size distribution curves of CFBFA, cement, gypsum, and hydrated lime.

2.2. Design of Experiments

2.2.1. Single Factor Variable Experiment

Cement can be used as a binder to assist the preparation of composite gravels. Cement can also be used as an alkaline activator to stimulate the activity of CFBFA. Adding hydrated lime to the reaction can further improve the activation of CFBFA by facilitating the availability of Ca^{2+}. In combination with a high concentration of OH^- ions, it can accelerate the dissolution of CFBFA grains, accelerating the hydration reaction. Gypsum not only acts as a catalyst in the hydration process of CFBFA, but also forms ettringite. Calcite is produced when ettringite is exposed to CO_2 in simulated flue gas. However, excessive use of gypsum may decrease the compressive strength of composite gravels as CFBFA is the primary reactant for both hydration and carbonation reactions, and increased gypsum content results in less CFBFA available for these reactions. In addition, excessive addition of gypsum will produce delayed ettringite, resulting in cracking of CFBFA composite gravels.

To investigate the effect of varying amounts of cement, hydrated lime, and gypsum on the mechanical properties of carbonated CFBFA composite gravels, we conducted compressive strength tests using different activator dosages.

2.2.2. Multi-Factor Variable Experiment

The purpose of this study was to determine the optimal conditions for enhancing the compressive strength of carbonated composite materials using BBD experiments while minimizing the number of required experiments. A total of 17 randomized experiments were conducted to investigate the effects of multiple factors acting simultaneously. The use of RSM allowed us to evaluate the interaction of factors and determine the optimal ratio for achieving the experimental goals. Statistical analysis, including analysis of variance (ANOVA), was performed on the model to ensure the validity of the results.

The study utilized Design-Expert 13.0 software (StatEase Inc., Minneapolis, MN, USA) to calculate the coefficients of the quadratic polynomial model and the optimization. To establish low, middle, and high levels for each variable, values of −1, 0, and 1 were, respectively, designated. The experimental domains, presented in Table 1 with their BBD encoded responses, included 12 factorial points with five replicates around the center point for error estimation purposes [15].

The experimental variables were transformed into coded values according to Equation (1):

$$X_i = (x_i - x_0)/\Delta x_i \quad (i = 1, 2, \cdots, k) \tag{1}$$

X_i denotes the coded value of an independent variable, while x_i represents its actual value. The value of the independent variable at the central point is denoted by x_0, and Δx_i is the magnitude of the step change. The BBD-RSM approach was employed to determine the connection between input variables and compressive strength by fitting experimental data with a quadratic multivariate mathematical equation, as expressed in Equation (2):

$$Y = \beta_0 + \sum \beta_i X_i + \sum \beta_{ii} X_i^2 + \sum \beta_{ij} X_i X_j \qquad (i, j = 1, 2, \cdots, k) \tag{2}$$

The predicted response, denoted as Y, which can be the compressive strength, was modeled using several terms, including the offset term β_0, linear effect β_i, squared effect β_{ii}, and interaction effect β_{ij}. X_i and X_j are the coded independent variables used in the model.

Based on the same dataset, ANN methods have been utilized for modeling the compressive strength of composite gravels. The prediction accuracy and performance of the ANN model are notably influenced by the number of hidden neurons; the optimal number is determined through trial and error. For this purpose, the number of hidden neurons varies from a minimum of 1 to a maximum of 20, and the optimal value is selected based on mean squared error (MSE) and coefficient of determination (R^2). The experimental design employed in the ANN model corresponds to the one used in the BBD-RSM model. To ensure unbiased results, the dataset is divided into three groups in a randomized manner, comprising training (75%), validation (15%), and test (15%) data sets. The predictive accuracy of the BBD-RSM and ANN models was assessed by root mean squared error (RMSE) and R^2 statistics. The GA approach was employed for the optimization of the ANN model. Finally, the results of composite gravel formulation optimization based on BBD-RSM and GA-ANN methods were compared with experiments to evaluate the accuracy of the results.

2.2.3. Mechanism Analysis

In order to examine the impact of various factors on the chemical and physical characteristics of the specimens, XRD, TGA, FTIR, and SEM analyses were conducted. For the X-ray diffraction analysis, a Rigaku Ultima IV (Instruments was purchased from Rigaku Electric Instruments (Beijing) Co., Ltd. in Beijing, China) with a CuKα source was used, and the scan was performed from 5° to 70° (2θ) with a sampling width of 0.02° and a scanning speed of 3°/min, while the generator was set at 40 kV/40 mA. The thermogravimetric results were obtained utilizing NETZSCH STA 449F5(Instruments was purchased from Brooke (Beijing) Technology Co., Ltd. in Beijing, China), and the heating rate was set at 10 °C/min over a temperature range of room temperature to 900 °C. To identify the functional group characteristics of the samples, a Bruker TENSOR II (Instruments was purchased from NETZSCH Scientific Instruments Trading (Shanghai) Ltd. in Shanghai, China) was utilized with a wavenumber range from 400 cm^{-1} to 4000 cm^{-1}. The SEM analysis was conducted using JEOL JSM-IT200(Instruments was purchased from JEOL (BEIJING) Co., Ltd. in Beijing, China).

3. Analyses

3.1. Single-Factor Analyses

In this study, cement, hydrated lime, and gypsum were investigated as influencing factors, and Figure 2. demonstrates their impact on compressive strength of 28 days. As the activator admixture increased for each individual factor, i.e., cement, hydrated lime, and gypsum, the compressive strength showed a steady increase. The highest compressive strength was achieved when the cement content was 20%, resulting in up to 4.06 MPa. The activity of CFBFA can be enhanced by calcium tricalcium silicate (C_3S) and calcium dicalcium silicate (C_2S) present in cement. This is due to the hydration of C_2S or C_3S in cement, which produces C-S-H and $Ca(OH)_2$ [32]. C_3S has a fast reaction rate, and it hydrates rapidly in water, releasing a large amount of heat, thus promoting the formation of early mechanical strength. C_2S hydration rate is relatively slow, and its hydration reaction is relatively mild, resulting in slower early mechanical strength formation. C_3S contributes to the rapid formation of early mechanical strength, due to its faster hydration rate, which is essential for the rapid curing of some cementitious materials. C_2S can not show a rapid increase in strength like C_3S in the early stage, but it has a certain contribution to the long-term mechanical strength development of cementitious materials. The hydration products of C_3S and C_2S mainly include C-S-H gels and calcium hydroxide (CH). But the hydration products of C_2S form relatively slowly. Moreover, when tricalcium aluminate (C_3A) in cement reacts with hydrating anhydrite in CFBFA, it forms ettringite. When the hydrated lime content is 10%, the compressive strength can reach 4.01MPa. Hydrated lime can break Si-O and Al-O bonds inside CFBFA, generate more C-(A)S-H gel, fill the pore structure inside the concrete, and increase the compressive strength of composite gravels. The highest compressive strength of only up to 1.51 MPa was achieved when the gypsum content was 20%. Gypsum has the ability to promote the hydration of volcanic ash-like materials. However, it is a neutral material. As a result, the volcanic ash activity of CFBFA may not be fully released. This can lead to a relatively small increase in intensity. In this system, CO_2 reacts with the hydration products, including $Ca(OH)_2$, C-(A)S-H and ettringite, to form calcite through carbonation.

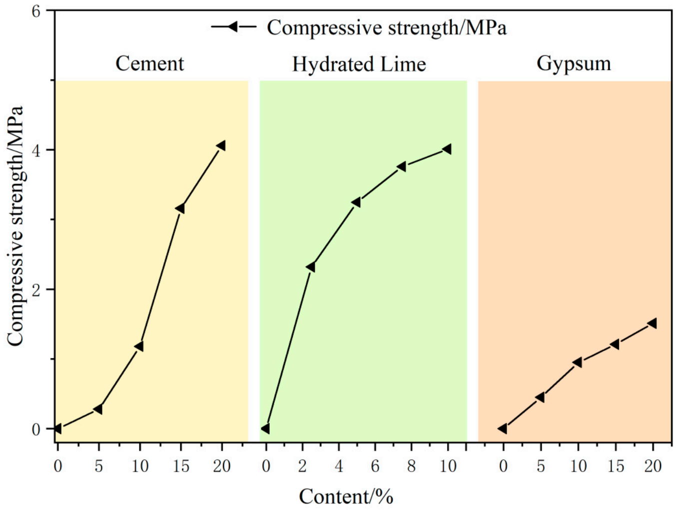

Figure 2. Influence of individual factors on compressive strength.

3.2. Modeling by BBD-RSM

The BBD method was utilized in this study, as outlined in Table 2, to acquire data and assist in process modeling. BBD is a response surface methodology that is based on the outcomes of a single-factor impact analysis. Each factor, including cement, hydrated lime, and gypsum, was allocated three different levels (−1, 0, and 1), and the actual variable levels were then established. This resulted in the formation of 17 experimental test formulations to examine the impact of each factor at the three different levels. Compressive strength models were employed to forecast the results, which were then compared to the actual values. Residual analysis was conducted to validate any discrepancies between the predicted and actual values. Table 2 presents the predicted and actual results for all the response variables analyzed in this investigation.

Table 2. Comparison of predicted and experimental results for RSM and ANN models.

Run	Real Variable Level			Compressive Strength/MPa				
	Cement/%	**Hydrated Lime/%**	**Gypsum/%**	**Actual**	**RSM**	**Error**	**ANN**	**Error**
1	15	5	10	12.11	12.34	0.0186	12.11	0
2	15	7.5	15	13.98	13.54	0.0315	13.71	0.2677
3	15	7.5	15	13.86	13.54	0.0231	13.71	0.1477
4	20	7.5	20	12.2	12.21	0.0006	12.20	0
5	15	7.5	15	13.26	13.54	0.0211	13.71	0.4523
6	15	10	20	10.58	10.36	0.0213	10.58	0
7	10	7.5	20	9.32	9.44	0.0126	9.32	0
8	10	5	15	11.32	11.10	0.0192	11.40	0.0768
9	15	5	20	11.28	11.38	0.0089	11.28	0
10	20	7.5	10	14.66	14.54	0.0080	14.66	0
11	20	5	15	14.46	14.35	0.0074	14.46	0
12	10	10	15	10.46	10.57	0.0103	10.46	0
13	20	10	15	14.01	14.23	0.0155	14.01	0
14	15	10	10	12.8	12.70	0.0078	12.80	0
15	15	7.5	15	13.29	13.54	0.0188	13.71	0.4223
16	15	7.5	15	13.31	13.54	0.0173	13.71	0.4023
17	10	7.5	10	10.41	10.40	0.0007	10.41	0

Figure 3 showcases both the predicted and actual compressive strength values. The color of the color point is determined by the compressive strength value. The warmer the color is, the larger the value is, and the cooler the color is, the smaller the value is. Based on the outcomes presented in Table 2, there is a high level of consistency between the predicted and actual compressive strength values within the designated range. These results serve as evidence of the BBD method's capacity to capture the influence of different factors on compressive strength. Additionally, a regression analysis was conducted, resulting in the creation of a second-order polynomial equation model for predicting compressive strength, represented by Equation (3).

$$\begin{aligned} Y = & -15.18875 + 1.103X_1 + 1.347X_2 + 1.9065X_3 + 0.0082X_1X_2 \\ & -0.0137X_1X_3 - 0.0278X_2X_3 - 0.02045X_1^2 - 0.0746X_2^2 - 0.05525X_3^2 \end{aligned} \tag{3}$$

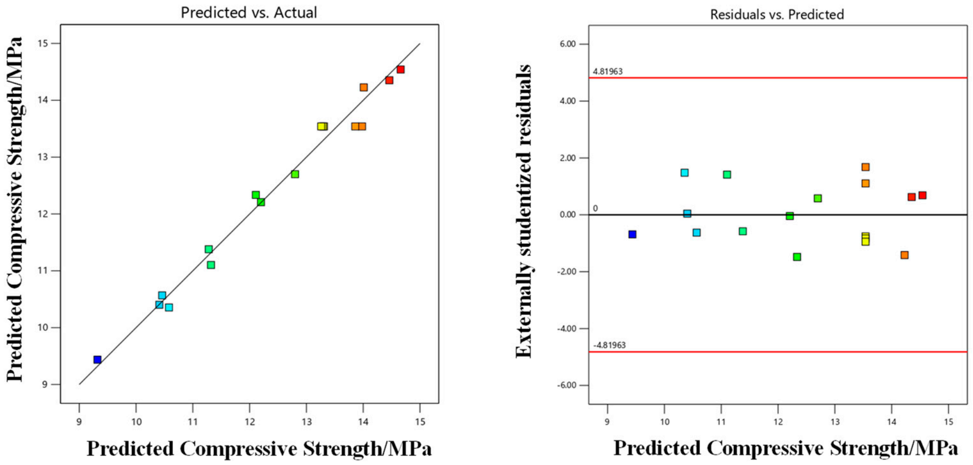

(a) Actual predicted compressive strength (b) Predicted compressive strength residuals

Figure 3. Comparing compressive strengths: Actual vs. Predicted.

In the equation, Y represents the predicted compressive strength, while X_1, X_2, and X_3 denote the coded values for cement, hydrated lime, and gypsum, respectively. Figure 3 shows both the predicted and actual compressive strength values. Figure 3a indicates that linear relationship between actual and predicted response variables. The computed values from the predictive model closely resembled the actual test values, indicating that the compressive strength prediction models accurately predicted the actual value. Figure 3b showcases the corresponding residual plots, revealing the even distribution of residuals and predicted values within a specific range for the compressive strength prediction models, which further supports the precision of the models.

3.3. Analysisising

To assess the fitness of the compressive strength equation, an ANOVA was conducted, and the results are presented in Table 3. The model's F-value was determined to be 42.55 ($p < 0.0001$), indicating that the model is dependable and a good fit throughout the regression zone. The *p*-value verifies the significance of the variables, reflecting the strength of the interplay among independent variables. A smaller *p*-value indicates greater significance of the corresponding variable. In this study, the *p*-values of X_1 and X_3 were less than 0.05 (Table 3), indicating that cement and gypsum have a significant impact on compressive strength. ANOVA (Table 3) revealed that the coding parameters X_{12}, X_{22}, and X_{32} were significant parameters, i.e., ($p > F$) < 0.05. The coefficient determination of R^2 was determined to be 0.9820, and the adjusted coefficient determination (R^2_{adj}) was calculated as 0.96. These values signify the high significance of the model.

Table 3. ANOVA analysis of the quadratic response surface model for compressive strength.

Variable	**Statistical Analysis**				
	Sum of Squares	**d*f***	**Mean Square**	**F-Value**	***p*-Value**
Model	41.39	9	4.60	42.55	<0.0001
X_1 (Cement)	23.87	1	23.87	220.91	<0.0001
X_2 (Hydrated Lime)	0.22	1	0.22	2.02	0.1987
X_3 (Gypsum)	5.45	1	5.45	50.38	0.0002
X_1 X_2	0.04	1	0.04	0.39	0.5527
X_1 X_3	0.47	1	0.47	4.34	0.0757
X_2 X_3	0.48	1	0.48	4.47	0.0723
X_1^2	1.10	1	1.10	10.18	0.0153
X_2^2	0.92	1	0.92	8.47	0.0227
X_3^2	8.03	1	8.03	74.33	<0.0001
Residual	0.76	7	0.11		
Lack of fit	0.27	3	0.09	0.73	0.5874
Pure error	0.49	4	0.12		
Cor Total	42.14	16			

$R^2 = 0.98$; $R^2_{adj} = 0.96$; $R^2_{pred} = 0.88$.

The ADEQ accuracy, which represents the ratio of effective signal to noise, was found to be 20.2472, indicating that the model is dependable and has an adequate signal response design. Furthermore, $R^2_{adj} - R^2_{pred} = 0.0784 < 0.2$, while C.V. was 2.64% < 10%, demonstrating high reliability and accuracy in this experiment. Referring to the predictive model for compressive strength, the predicted maximum attained was 14.992 MPa, achieved through the optimal composition of cement: hydrated lime: gypsum = 19.94%: 7.748%: 13.118%.

The response surface analysis method employs contour plots to provide valuable insight into the significance of the interaction between different factors. In particular, an elliptical contour shape indicates a significant interaction between factors, while a circular shape implies an insignificant interaction. Based on the contour plot, it is evident that the interaction between cement content and hydrated lime content is significant, while the interaction between cement content and gypsum content, as well as between hydrated lime and gypsum content, is less significant. The color of the area in response surface analysis and contour plots of Figures 4–6 is determined by the compressive strength value, and the warmer the color, the larger the value.

Figure 4 shows response surface and contour plots that demonstrate the influence of cement and hydrated lime contents on compressive strength, with 15% gypsum content. The plots reveal that the addition of hydrated lime initially enhances the compressive strength of the composite gravels, up to a peak value at around 7.5%. However, further increases in hydrated lime content leads to a decline in compressive strength. On the other hand, cement content has a linear effect on the response, with an increase in cement content resulting in a sharp rise in compressive strength.

The $Ca(OH)_2$ produced by the hydration of cement will react with CFBFA in a volcanic ash reaction, called the second hydration [14]. Sufficient $Ca(OH)_2$ is crucial for this reaction to occur, and adding hydrated lime helps address the issue of insufficient $Ca(OH)_2$ in the cementitious system. However, a competitive relationship emerges between the volcanic ash reaction and cement hydration, with the presence of hydrated lime inhibiting cement hydration. Consequently, there exists an optimal dosage of additional hydrated lime. Under this optimal dosage, a balance is achieved between the pozzolanic reaction and cement hydration, leading to a higher content of hydration products. As a result, the composite gravels exhibit a denser microstructure and improved mechanical properties. The main component of cement C_2S,C_3S hydration product is $Ca(OH)_2$; it is the raw material of carbonization reaction. C-S-H gel produced by pozzolanic reaction between hydrated lime and CFBFA is carbonized material. The sulfur contained in CFBFA will form ettringite with the Al-containing substance, which is also carbonized raw material. $Ca(OH)_2$, C-S-H gel, and ettringite can carbonize with CO_2 to produce carbonizing products such as calcite. Moreover, the addition of gypsum can promote the carbonation depth and increase the adsorption rate of CO_2. Carbonation can refine the pore structure and increase mechanical strength through the precipitation of calcite in the pores of the cementitious material.

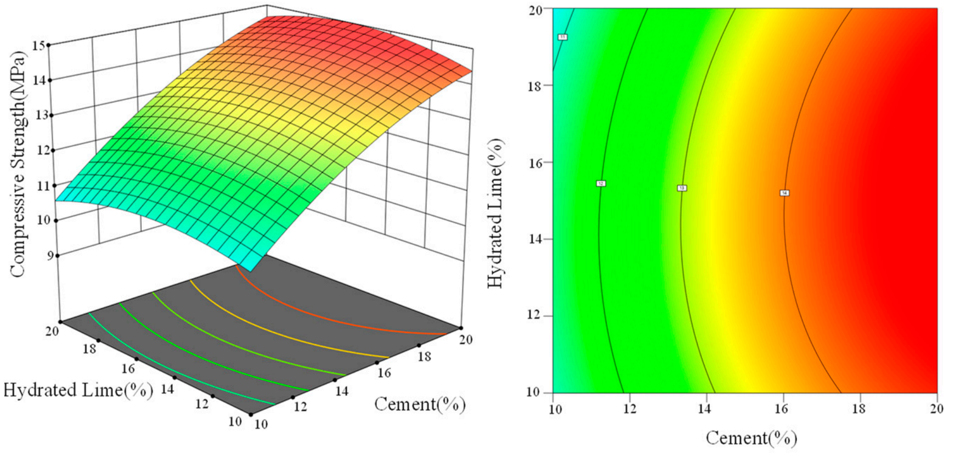

Figure 4. Response surface analysis plot and contour plot revealing the impact of cement and hydrated lime at 15% gypsum level on compressive strength.

Upon examination of the contour plot in Figure 5, it can be observed that there is a distinct area where the optimal compressive strength can be achieved. This area is characterized by a hydrated lime content between 7% and 8% and a gypsum content between 12% and 16%, where the maximum compressive strength is attained.

CFBFA, when activated solely by $Ca(OH)_2$, primarily produces hydration products such as C-(A)-S-H gels. However, when CFBFA is co-activated by hydrated lime and gypsum, it can generate ettringite in the cementitious material. The presence of ettringite further contributes to the improvement of the mechanical properties of the composite gravels. However, excessive hydrated lime addition can result in an counter alkali reaction.

Excessive amounts of gypsum can lead to the formation of delay ettringite, causing volume expansion and composite gravels cracking. Thus, there exists an optimal addition ratio of gypsum and hydrated lime to avoid these issues.

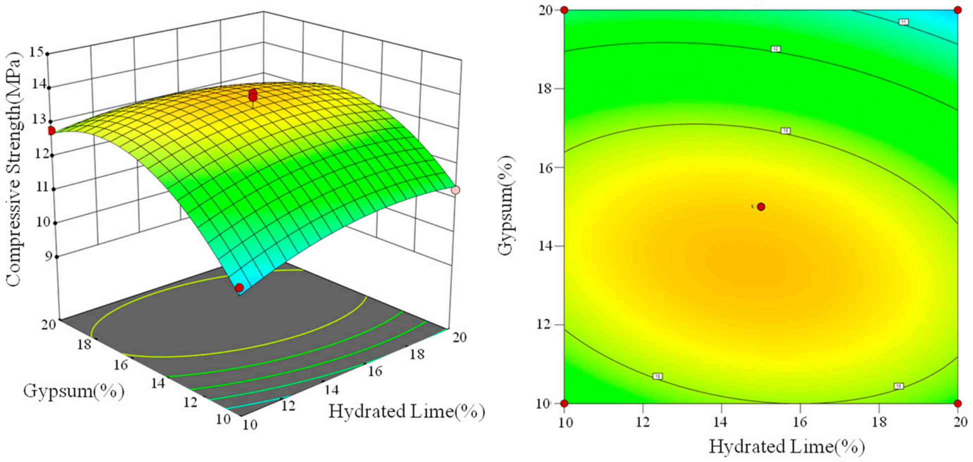

Figure 5. Response surface analysis plot and contour plot revealing the impact of gypsum and hydrated lime at 15% cement level on compressive strength.

The response surface and contour plots presented in Figure 6 provide insights into the influence of cement and gypsum contents on compressive strength, with a fixed hydrated lime content of 7.5%. The results indicate that an increase in cement content initially enhanced the compressive strength, while a decrease in gypsum content had a similar effect. Nevertheless, as the cement content continued to rise and gypsum content continued to decrease, the rate of improvement in compressive strength gradually diminished.

Gypsum has a catalytic effect on the hydration of cement and can also play a role in retarding the setting of C_3A in cement. Gypsum also reacts with $Ca(OH)_2$ and the aluminum-containing phase produced by cement hydration to produce ettringite [33]. By growing inside the cementitious material, ettringite continuously fill the pores, improve the material compactness and improve the mechanical properties of the composite gravels. However, excess gypsum can lead to the production of excess ettringite, resulting in swelling and cracking. Therefore, cement and gypsum have an optimal ratio to ensure that the gypsum has the best activation effect.

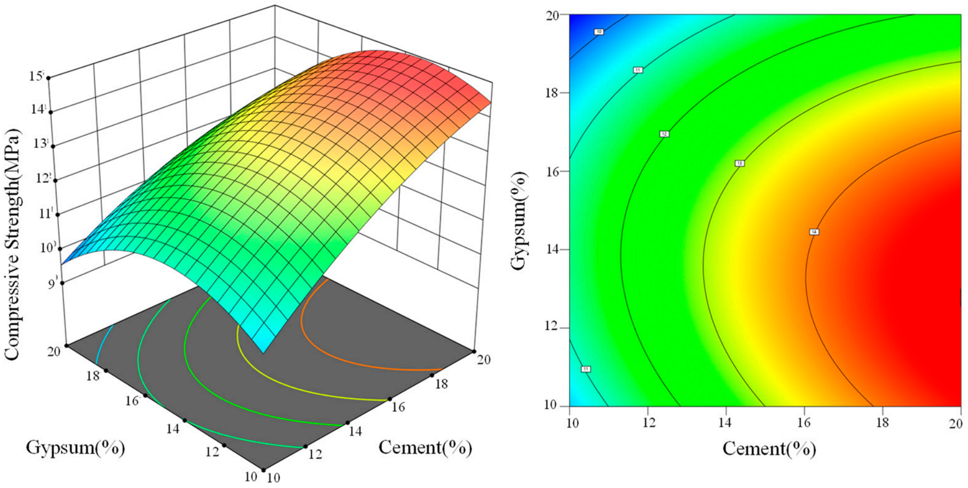

Figure 6. Response surface analysis plot and contour plot revealing the impact of cement and gypsum at 7.5% hydrated lime level on compressive strength.

The above analysis can conclude that pairwise activators have synergistic effects. However, activation by only two activators is not enough. CFBFA activated only by cement and hydrated lime produced less ettringite. CFBFA activated only by cement and gypsum cannot be fully activated. CFBFA activated only by lime and gypsum lacks binders. Cement is not only an activator, but also a binder. Therefore, triple activator is better than double activator.

3.4. Modeling by GA-ANN

In this study, an intelligent algorithmic model was developed to optimize the proportioning of strength and achieve precise predictions. The data set presented in Table 2 was modeled using the ANN method. Topology is a crucial hyperparameter in neural networks, and it plays a significant role in network performance [34]. Determining the optimal number of hidden layer neurons is one of the critical challenges in building an artificial neural network topology [35]. To address this challenge, the number of hidden neurons was varied from 1 to 20 to identify the optimal number of neurons that yield the lowest Mean Squared Error (MSE) value and R-squared (R^2) value closest to 1. These findings indicate that the model with 10 hidden neurons accurately represents the nonlinear relationship between each influencing factor and the compressive strength and has an outstanding predictive effect on the composite gravel strength.

The most appropriate neural network model architecture was determined to be the 3-10-1 topology, as illustrated in Figure 7. The accuracy of the model was evaluated using R^2 values in Figure 8. The results demonstrated excellent accuracy with values of 0.9932. These results suggest a strong correlation between the predicted and experimental compressive strength, indicating the high accuracy of the model in predicting experimental data.

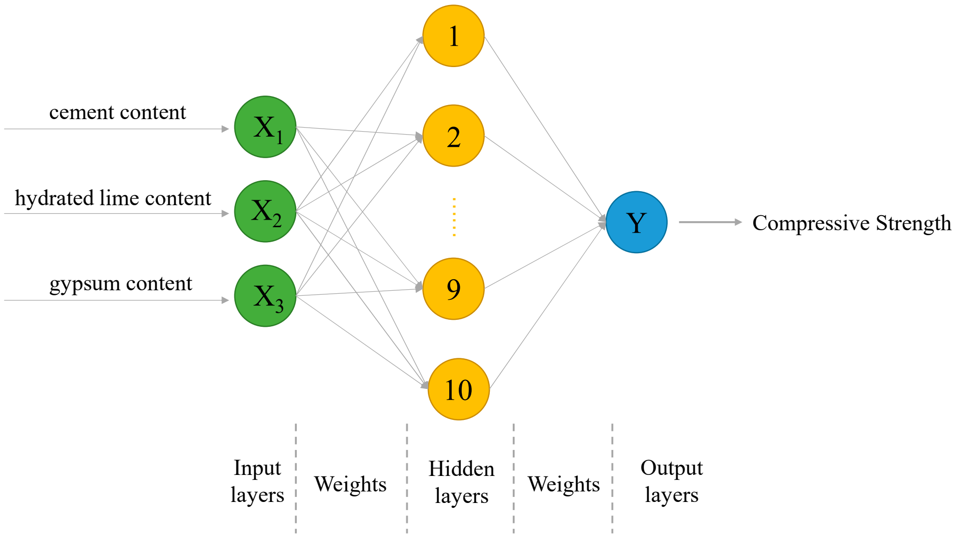

Figure 7. Visualization of Artificial Neural Network (ANN) topology.

GA is a widely used computational model for finding optimal solutions. It is based on the principles of biological evolution and simulates natural selection and inheritance. In this study, the output of the trained artificial neural network, which represents the compressive strength of the composite gravel, is utilized as the fitness function of the genetic algorithm. The genetic algorithm optimizes the addition conditions of cement, hydrated lime, and gypsum by converging towards the individual with the highest fitness value, i.e., the individual with the highest compressive strength (refer to Figure 9). Through optimization of the addition conditions of cement, hydrated lime, and gypsum, the compressive strength of the composite gravel was increased to 14.9 MPa.

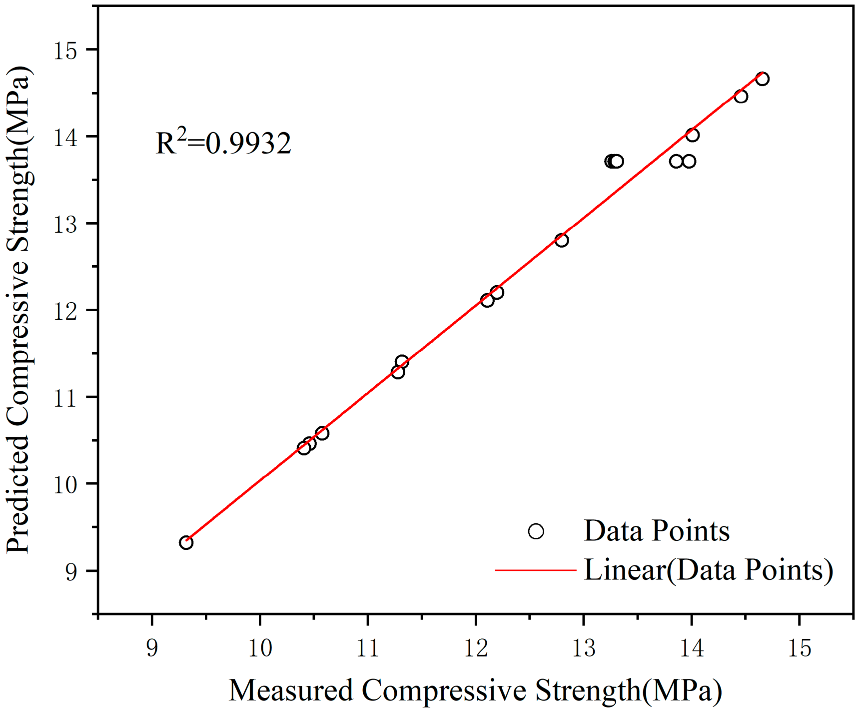

Figure 8. Regression analysis and comparison of experimental data with BP-ANN model simulated values.

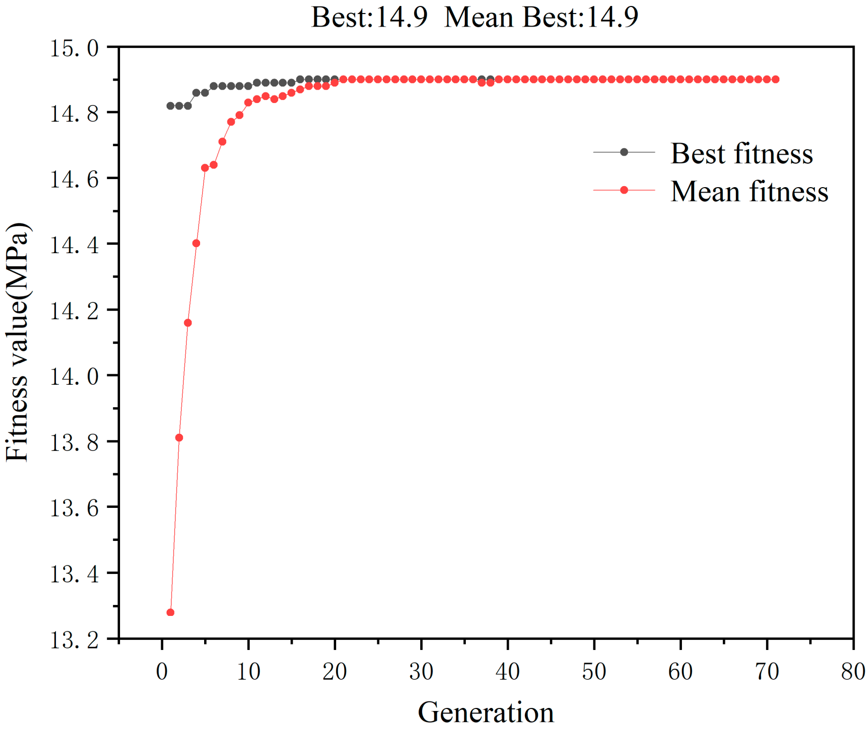

Figure 9. Evolutionary fitness progression across 70 generations.

3.5. Comparative Analysis of BBD-RSM and GA-ANN Techniques

The coefficient of determination (R^2) is a widely used statistical measure to assess the quality of predictions. It quantifies how well a linear model fits the observed data. As can be seen from Table 4, the R^2 between the predicted and experimental values of the RSM model and ANN model are 0.9820 and 0.9932, respectively. The ANN model gives lower predicted RMSE values compared to the RSM model [36]. It is confirmed that the error bias of ANN prediction is smaller. The results demonstrate that the ANN model yields predicted values that exhibit a higher degree of proximity to the experimental values. The GA-ANN and BBD-RSM models exhibit relative errors of 1.22% and 2.76%, respectively, in predicting the compressive strength of composite gravels. These results indicate that GA-ANN has higher accuracy and reliability in modeling and optimizing the parameter interactions associated with the compressive strength of composite gravels. Furthermore, each model possesses its unique advantages. The RSM illustrates how factors interact to influence the compressive strength of composite gravels and offers graphical visualizations to interpret the relationship between the independent variables and the response values. Moreover, the method presents the advantage of requiring a limited number of experiments to yield substantial information, resulting in time and cost savings. However, it is constrained by its ability to provide solely first- or second-order polynomial models. In contrast, artificial neural networks have the capability to model nonlinear relationships of any form. As a black-box model, they do not rely on experimental design to establish explicit relationships. Consequently, artificial neural networks overcome the challenges associated with experimental design and offer a more flexible approach.

Table 4. Comparative analysis of experimental validation and predicted results between BBD-RSM and GA-ANN techniques.

Variables	**BBD-RSM**		**GA-ANN**	
	Predicted Contents	**Experimental Contents**	**Predicted Contents**	**Experimental Contents**
Cement	19.94	20	20	20
Hydrated Lime	7.748	7.7	5.648	5.6
Gypsum	13.118	13	12.817	12.8
Compressive Strength	14.992	14.59	14.9	14.72
Relative Error (%)	2.76%		1.22%	
R^2	0.9820		0.9932	
RMSE	0.21		0.19	

3.6. Internal Mechanism Analysis

In order to gain a more comprehensive understanding of the factors that affect the compressive strength of composite gravels, analyses were conducted on the chemical and physical characteristics of the control group (pure CFBFA), single-factor groups, as well as the optimization group. The results of the analysis showed that the optimization group exhibited the most significant enhancements in compressive strength.

3.6.1. XRD Analysis

Figure 10 shows the results of XRD analysis. The X-ray diffraction (XRD) spectrum indicates that the pure CFBFA group produced few hydration products due to the weak alkalinity. Since the C-S-H gel structure is amorphous, no diffraction peak was observed in the XRD pattern. The characteristic peaks of quartz and anhydrite in CFBFA are observed. The XRD analysis of the 20% gypsum group closely resembles that of the control group, with a distinct gypsum peak observed. This suggests that the majority of gypsum does not actively participate in the hydration reaction. This can be attributed to the neutral nature of gypsum as an activator, resulting in limited excitation effects. The presence of calcite peaks in both groups is attributed to the carbonation reaction of CaO in the CFBFA, as indicated in Formulas (4) and (12).

In the 20% cement group, the alkaline activator can promote anhydrite hydration to generate gypsum, as shown in Formula (5). The reaction between C_3A in cement and gypsum led to the formation of ettringite, as shown in the Formula (6) [37]. C_2S and C_3S in cement produce C-S-H gel and $Ca(OH)_2$ through hydration, as shown in Formulas (7) and (8). The $Ca(OH)_2$ reacts with Al_2O_3(active) and gypsum to form ettringite, as shown in Formula (9).

The 10% hydrated lime group will also produce the reaction in Formula (9) [38]. In the optimization group, cement, hydrated lime, and gypsum showed synergistic effects. The disappearance of the anhydrite peak suggests that the addition of composite activators facilitated the hydration of anhydrite, as indicated in Formula (5). Cement undergoes hydration reaction with CFBFA. Hydrated lime is introduced to increase the alkalinity, effectively supplementing the required $Ca(OH)_2$ for pozzolanic reactions. Gypsum contributes to the stimulation of reactions. Gypsum also provides ${SO_4}^{2-}$ to form ettringite. The figure shows that the peak value of ettringite increased significantly. The combination of these constituents synergistically influences the hydration and carbonation reaction in the cementitious system, contributing to its improved performance and properties. Calcite can be generated from C_2S and C_3S in cement, as shown in Formulas (10) and (11). Calcite is mainly generated from the hydration products $Ca(OH)_2$, C-S-H gel and ettringite(AFt), as shown in Formulas (12)–(14) [39]. The peak of calcite increased significantly since a large amount of hydration products can be produced in the optimization group.

$$\mathrm{CaO + H_2O \rightarrow Ca(OH)_2} \tag{4}$$

$$\mathrm{CaSO_4 + 2H_2O \rightarrow CaSO_4 \cdot 2H_2O} \tag{5}$$

$$\mathrm{3CaO \cdot Al_2O_3(C_3A) + 3CaSO_4{\cdot}H_2O + 26H_2O \rightarrow 3CaO \cdot Al_2O_3 \cdot 3CaSO_4{\cdot}32H_2O(AFt)} \tag{6}$$

$$\mathrm{C_3S + H_2O \rightarrow C - S - H + Ca(OH)_2} \tag{7}$$

$$\mathrm{C_2S + H_2O \rightarrow C - S - H + Ca(OH)_2} \tag{8}$$

$$\mathrm{3Ca(OH)_2 + Al_2O_3(active) + 3CaSO_4 \cdot 2H_2O + 23H_2O \rightarrow 3CaO \cdot Al_2O_3 \cdot 3CaSO_4{\cdot}32H_2O(AFt)} \tag{9}$$

$$\mathrm{3CaO \cdot SiO_2 + 3CO_2 + H_2O \rightarrow 3CaCO_3 + SiO_2 \cdot nH_2O} \tag{10}$$

$$\mathrm{2CaO \cdot SiO_2 + 2CO_2 + H_2O \rightarrow 2CaCO_3 + SiO_2 \cdot nH_2O} \tag{11}$$

$$\mathrm{Ca\left(OH\right)_2 + CO_3^{2-} + 2H^+ \rightarrow CaCO_3 + 2H_2O} \tag{12}$$

$$\mathrm{3CaO \cdot 2SiO_2 \cdot 3H_2O(C - S - H) + CO_3^{2-} + H^+ \rightarrow 3CaCO_3 \cdot 2SiO_2 \cdot 3H_2O} \tag{13}$$

$$\mathrm{3CaO \cdot Al_2O_3 \cdot 3CaSO_4{\cdot}32H_2O(AFt) + 3CO_2 + H_2O \rightarrow 3CaCO_3 + 3CaSO_4 + Al_2O_3 \cdot nH_2O} \tag{14}$$

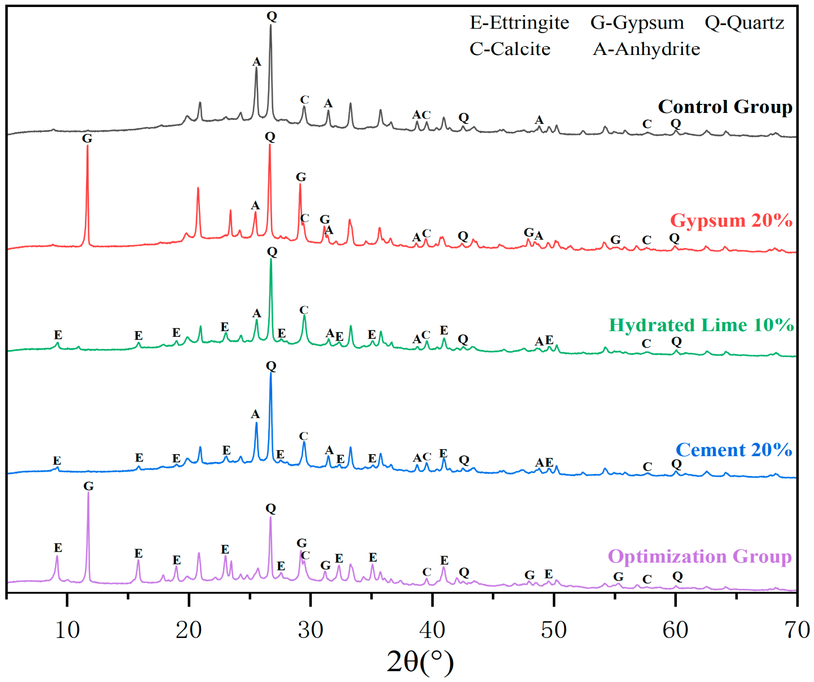

Figure 10. XRD characterization of samples.

3.6.2. TG-DTG Analysis

The evaporation of interlayer water occurs at temperatures below 240 °C. Hydroxyl groups within the structure undergo a loss between 240 °C and 500 °C. Mass loss between 500 °C and 800 °C is mainly attributed to decarburization of $CaCO_3$, while the losses above 800 °C are primarily caused by the loss of SO_3 in gypsum [40].

Figure 11 presents the TG-DTG analysis results of the specimen after 28 days of curing. Hydration products were formed in the cement, hydrated lime, and optimization groups, while almost no hydration products were formed in the control and gypsum groups.

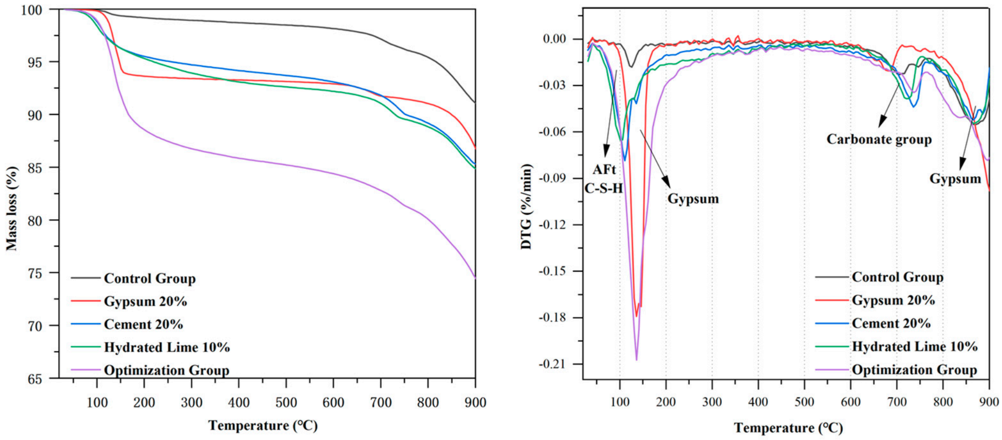

Figure 11. TGA and its derivate (DTG) of samples.

The carbon content of the control group, 20% gypsum, 10% hydrated lime, 20% cement, and optimization group after carbonation was 1.91%, 1.98%, 3.01%, 3.53%, and 3.61%, respectively. The combined excitation promoted the carbonation of CFBFA, with the relative amount of CO_2 absorbed by CFBFA in the five samples being optimization group > 20% cement > 10% hydrated lime > 20% gypsum > control group. This verifies the results of XRD analysis.

3.6.3. FTIR Analysis

Figure 12 shows the results of the FTIR analysis. FTIR analysis confirmed and complemented the results of XRD analysis. The CFBFA sample exhibits an absorption peak at 474 cm^{-1} which can be attributed to the Si-O-Si bending vibration of quartz [35]. The strong and broad band observed at 781 cm^{-1} is associated with the symmetric stretching vibration of Si-O-Si and AlO_4 in quartz, present in the CFBFA [41]. The symmetric stretching vibrations of Al-O-Si are observed at 561 cm^{-1} and are attributed to biased kaolinite in the CFBFA [42]. However, in the optimization group, these peaks are significantly weakened due to the breakage of their chemical bonds by ternary activator.

The band observed between 3408 and 3545 cm^{-1} corresponds to the stretch band in the water molecule of the hydration product [43]. It can be seen that each group has some hydration, but the control group exhibits the weakest hydration due to the weak pozzolanic activity of the unexcited CFBFA.

The absorption peaks at 874 cm^{-1} and 1420–1480 cm^{-1} correspond to calcite bending vibrations in CO_3^{2-} due to composite gravel carbonation, with the latter peak indicating C-O symmetric stretching vibrations. The cement and hydrated lime groups exhibit absorption peaks at 3620 cm^{-1} due to the hydroxyl groups in $Ca(OH)_2$. The optimal and gypsum groups exhibit absorption peaks at 1600 cm^{-1}, representing the stretching and bending vibration bands of water molecules in gypsum [44]. Furthermore, the absorption peak observed only at 1686 cm^{-1} represents water of crystallization in the ettringite, indicating that the optimization group and gypsum group produces more ettringite.

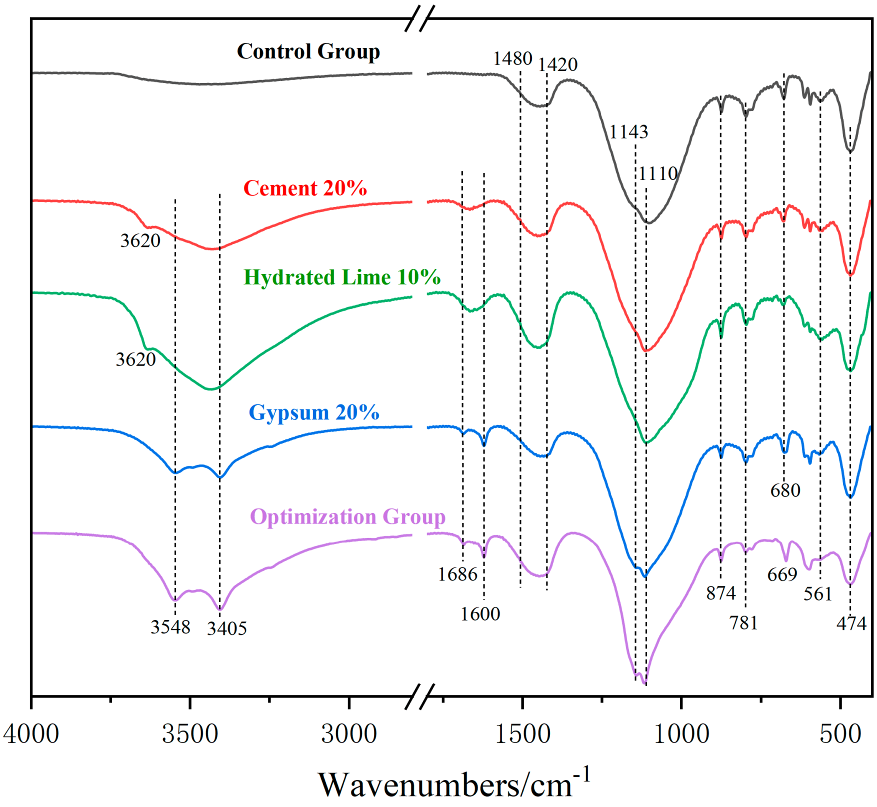

Figure 12. FTIR spectral analysis.

The presence of Q3 and Q4 units are possible in C–S–H gels in carbonated samples [45–47]. The bands at 1110 cm^{-1} and 1143 cm^{-1} are typical bands of Q3 and Q4 sites assigned to C-S-H with higher SiO_2 content [48].

The absorption peaks observed at 680 cm^{-1} correspond to the in-plane bending vibrations of SO_4^{2-} in anhydrite. The figure shows that unhydrated anhydrite is still present in the cementitious material excited by a single activator. The hydration of anhydrite can be stimulated by the ternary activator. In the optimization group, the characteristic absorption peak of the AlO_6 octahedron in the monocarbonate, ettringite is observed at 669 cm^{-1} [49]. This also proves that the optimization group produces more ettringite.

3.6.4. Microstructural Analysis

Figure 13 displays the scanning electron microscopy (SEM) images of the control group, 20% cement group, 10% hydrated lime group, 20% gypsum group, and optimization group captured at 5000× magnification and are depicted in Figure 13. Sample group names are listed in the top left corner of the picture. Figure 13a shows a SEM plot of the CFBFA revealing a large number of CFBFA particles with rough morphology and poor microstructure. The addition of 20% gypsum to the CFBFA (Figure 13b) leads to the release of the pozzolanic activity of CFBFA slightly, resulting in the formation of a small amount of C-S-H gel [12]; Figure 13c,d illustrate the SEM images captured after adding 20% cement and 10% hydrated lime, respectively, where a large amount of C-S-H gel and a small amount of ettringite are produced. Figure 13e shows the SEM image of the optimization group where the mixture of cement, hydrated lime, and gypsum significantly excites CFBFA activity to generate a large number of hydration products, leading to the formation of a dense and optimized pore structure with interwoven flocculent C-S-H gels and needle-rod ettringite, which is consistent with the compressive strength test results.

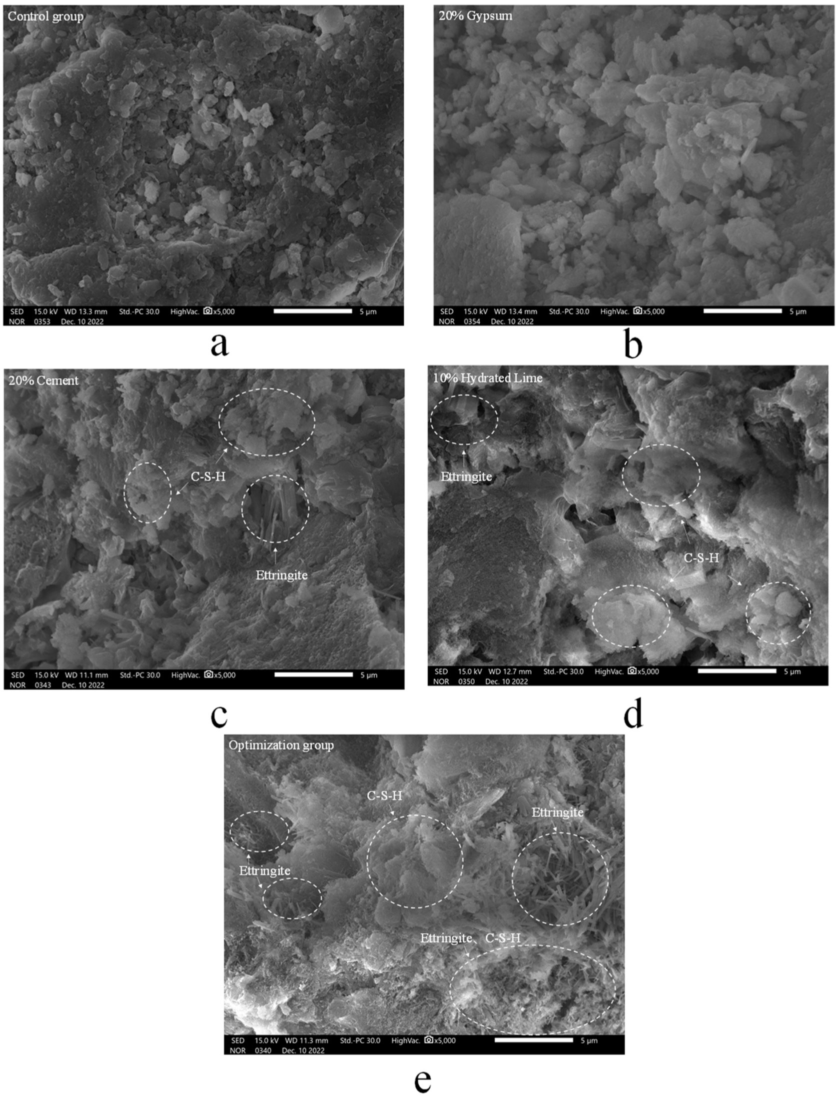

Figure 13. Microstructures of samples.

4. Conclusions

1. BBD-RSM and GA-ANN can be employed for statistical modeling and optimization of the compressive strength of composite gravels. These two numerical analysis methods have their own advantages. ANN predicts more accurately than RSM, with R^2 of 0.9932 and 0.9820, respectively.
2. The RSM model can be applied to describe the interaction effect between the pairwise activators. CFBFA activated only by cement and lime produced less ettringite. CFBFA activated only by cement and gypsum cannot be fully activated. CFBFA activated only by hydrated lime and gypsum lacks binders. Binary activator is not as effective as the ternary activator.
3. The utilization of XRD and FTIR characterization techniques revealed that the combined action of the three activators resulted in the generation of abundant hydration products. Cement undergoes pozzolanic reaction with CFBFA. The alkalinity of cement is not enough to activate large amounts of CFBFA. Hydrated lime is introduced to increase the alkalinity, effectively supplementing the required $Ca(OH)_2$ for pozzolanic reactions. Gypsum provides $SO_4{}^{2-}$ to form ettringite. The ternary activator synergistically influences the overall hydration and carbonation transformations in the cementitious system, contributing to its improved performance and properties.

4. The utilization of TG-DTG characterization techniques revealed that the CO_2 curing process resulted in the generation of significant amounts of calcite, improving the mechanical properties of the material. The optimization group generated the most hydration products and carbonation products.
5. The application of SEM characterization techniques unveiled that the synergistic action of the ternary activator led to a strong activation of CFBFA, resulting in the needle and rod-shaped ettringite intertwined with a substantial quantity of flocculent C-S-H gel. The existence of this interwoven structure makes the microstructure compact and the pore structure optimized. These characterization findings are consistent with the experimental results of uniaxial unconfined compressive strength.

Author Contributions: All authors contributed to the study conception and design. Material preparation, data collection and analysis were performed by S.M., N.W. and Y.F. The first draft of the manuscript was written by N.X. and all authors commented on previous versions of the manuscript. All authors have read and agreed to the published version of the manuscript.

Funding: This work was funded by the National Key Research and Development Program of China (2020YFB0606300).

Data Availability Statement: Data will be made available on request.

Conflicts of Interest: The authors declare no conflict of interest.

References

1. Jang, J.G.; Park, S.-M.; Chung, S.; Ahn, J.-W.; Kim, H.-K. Utilization of circulating fluidized bed combustion ash in producing controlled low-strength materials with cement or sodium carbonate as activator. *Constr. Build. Mater.* **2018**, *159*, 642–651. [CrossRef]
2. Cheng, A.; Hsu, H.-M.; Chao, S.-J. Properties of concrete incorporating bed ash from circulating fluidized bed combustion and ground granulates blast-furnace slag. *J. Wuhan Univ. Technol. Sci. Ed.* **2011**, *26*, 348–354. [CrossRef]
3. Chen, X.; Yan, Y.; Liu, Y.; Hu, Z. Utilization of circulating fluidized bed fly ash for the preparation of foam concrete. *Constr. Build. Mater.* **2014**, *54*, 137–146. [CrossRef]
4. Li, X.-G.; Chen, Q.-B.; Huang, K.-Z.; Ma, B.-G.; Wu, B. Cementitious properties and hydration mechanism of circulating fluidized bed combustion (CFBC) desulfurization ashes. *Constr. Build. Mater.* **2012**, *36*, 182–187. [CrossRef]
5. Nguyen, H.-A.; Chang, T.-P.; Shih, J.-Y.; Chen, C.-T.; Nguyen, T.-D. Influence of circulating fluidized bed combustion (CFBC) fly ash on properties of modified high volume low calcium fly ash (HVFA) cement paste. *Constr. Build. Mater.* **2015**, *91*, 208–215. [CrossRef]
6. Park, S.M.; Lee, N.K.; Lee, H.K. Circulating fluidized bed combustion ash as controlled low-strength material (CLSM) by alkaline activation. *Constr. Build. Mater.* **2017**, *156*, 728–738. [CrossRef]
7. Koukouzas, N.; Ketikidis, C.; Itskos, G.; Spiliotis, X.; Karayannis, V.; Papapolymerou, G. Synthesis of CFB-Coal Fly Ash Clay Bricks and Their Characterisation. *Waste Biomass Valorization* **2011**, *2*, 87–94. [CrossRef]
8. Huang, J.; Chen, H.; Yang, J.; Zhou, T.; Zhang, H. Effects of particle size on microstructure and mechanical strength of a fly ash based ceramic membrane. *Ceram. Int.* **2023**, *49*, 15655–15664. [CrossRef]
9. Qin, J.; Cui, C.; Cui, X.; Hussain, A.; Yang, C. Preparation and characterization of ceramsite from lime mud and coal fly ash. *Constr. Build. Mater.* **2015**, *95*, 10–17. [CrossRef]
10. Jia, G.; Wang, Y.; Yang, F.; Ma, Z. Preparation of CFB fly ash/sewage sludge ceramsite and the morphological transformation and release properties of sulfur. *Constr. Build. Mater.* **2023**, *373*, 130864. [CrossRef]
11. Xu, F.; Liu, W.; Bu, S.; Zhang, L.; Fang, J.; Yu, Z.; Xu, W.; Ding, H.; Huo, G. Manufacturing non-sintered ceramsite from incinerated municipal solid waste ash (IMSWA): Production and performance. *Process. Saf. Environ. Prot.* **2022**, *163*, 116–130. [CrossRef]
12. Li, D.; Sun, R.; Wang, D.; Ren, C.; Fang, K. Study on the pozzolanic activity of ultrafine circulating fluidized-bed fly ash prepared by jet mill. *Fuel* **2021**, *291*, 120220. [CrossRef]
13. Yang, J.; Hu, H.; He, X.; Su, Y.; Wang, Y.; Tan, H.; Pan, H. Effect of steam curing on compressive strength and microstructure of high volume ultrafine fly ash cement mortar. *Constr. Build. Mater.* **2021**, *266*, 120894. [CrossRef]
14. Zhang, G.; Peng, G.-F.; Zuo, X.-Y.; Niu, X.-J.; Ding, H. Adding hydrated lime for improving microstructure and mechanical properties of mortar for ultra-high performance concrete. *Cem. Concr. Res.* **2023**, *167*, 107130. [CrossRef]
15. Li, Z.; Wang, X.; Hou, Y.; Wu, Z. Optimization of mechanical properties and water absorption behavior of building gypsum by ternary matrix mixture. *Constr. Build. Mater.* **2022**, *350*, 128910. [CrossRef]
16. Illikainen, M.; Tanskanen, P.; Kinnunen, P.; Körkkö, M.; Peltosaari, O.; Wigren, V.; Österbacka, J.; Talling, B.; Niinimäki, J. Reactivity and self-hardening of fly ash from the fluidized bed combustion of wood and peat. *Fuel* **2014**, *135*, 69–75. [CrossRef]
17. Watanabe, A.; Furukawa, H.; Miyamoto, S.; Minagawa, H. Non-destructive chemical analysis of water and chlorine content in cement paste using near-infrared spectroscopy. *Constr. Build. Mater.* **2019**, *196*, 95–104. [CrossRef]

18. Iribarne, J.; Iribarne, A.; Blondin, J.; Anthony, E. Hydration of combustion ashes—A chemical and physical study. *Fuel* **2001**, *80*, 773–784. [CrossRef]
19. Moghal, A.A.B.; Rehman, A.U.; Vydehi, K.V.; Umer, U. Sustainable Perspective of Low-Lime Stabilized Fly Ashes for Geotechnical Applications: PROMETHEE-Based Optimization Approach. *Sustainability* **2020**, *12*, 6649. [CrossRef]
20. Kursuncu, B.; Gencel, O.; Bayraktar, O.Y.; Shi, J.; Nematzadeh, M.; Kaplan, G. Optimization of foam concrete characteristics using response surface methodology and artificial neural networks. *Constr. Build. Mater.* **2022**, *337*, 127575. [CrossRef]
21. Lv, S.; Yuan, J.; Peng, X.; Cabrera, M.B.; Guo, S.; Luo, X.; Gao, J. Performance and optimization of bio-oil/Buton rock asphalt composite modified asphalt. *Constr. Build. Mater.* **2020**, *264*, 120235. [CrossRef]
22. Hacene, S.M.A.B.; Ghomari, F.; Schoefs, F.; Khelidj, A. Probabilistic Modelling of Compressive Strength of Concrete Using Response Surface Methodology and Neural Networks. *Arab. J. Sci. Eng.* **2014**, *39*, 4451–4460. [CrossRef]
23. Junyan, L.; Qingju, T.; Xun, L.; Yang, W. Research on the quantitative analysis of subsurface defects for non-destructive testing by lock-in thermography. *NDT E Int.* **2012**, *45*, 104–110. [CrossRef]
24. Getahun, M.A.; Shitote, S.M.; Abiero Gariy, Z.C. Artificial neural network based modelling approach for strength prediction of concrete incorporating agricultural and construction wastes. *Constr. Build. Mater.* **2018**, *190*, 517–525. [CrossRef]
25. Kittinaraporn, W.; Tuprakay, S.; Prasittisopin, L. Effective Modeling for Construction Activities of Recycled Aggregate Concrete Using Artificial Neural Network. *J. Constr. Eng. Manag.* **2022**, *148*, 04021206. [CrossRef]
26. Guo, H.; Shi, C.; Guan, X.; Zhu, J.; Ding, Y.; Ling, T.-C.; Zhang, H.; Wang, Y. Durability of recycled aggregate concrete—A review. *Cem. Concr. Compos.* **2018**, *89*, 251–259. [CrossRef]
27. Shi, C.; He, F.; Wu, Y. Effect of pre-conditioning on CO2 curing of lightweight concrete blocks mixtures. *Constr. Build. Mater.* **2012**, *26*, 257–267. [CrossRef]
28. Lu, B.; Shi, C.; Cao, Z.; Guo, M.; Zheng, J. Effect of carbonated coarse recycled concrete aggregate on the properties and microstructure of recycled concrete. *J. Clean. Prod.* **2019**, *233*, 421–428. [CrossRef]
29. Johannesson, B.; Utgenannt, P. Microstructural changes caused by carbonation of cement mortar. *Cem. Concr. Res.* **2001**, *31*, 925–931. [CrossRef]
30. Monkman, S.; Kenward, P.A.; Dipple, G.; MacDonald, M.; Raudsepp, M. Activation of cement hydration with carbon dioxide. *J. Sustain. Cem. Mater.* **2018**, *7*, 160–181. [CrossRef]
31. Zhan, B.J.; Poon, C.S.; Shi, C.J. Materials characteristics affecting CO_2 curing of concrete blocks containing recycled aggregates. *Cem. Concr. Compos.* **2016**, *67*, 50–59. [CrossRef]
32. Wu, T.; Chi, M.; Huang, R. Characteristics of CFBC fly ash and properties of cement-based composites with CFBC fly ash and coal-fired fly ash. *Constr. Build. Mater.* **2014**, *66*, 172–180. [CrossRef]
33. Neto, A.A.M.; Cincotto, M.A.; Repette, W. Mechanical properties, drying and autogenous shrinkage of blast furnace slag activated with hydrated lime and gypsum. *Cem. Concr. Compos.* **2010**, *32*, 312–318. [CrossRef]
34. Adesanya, E.; Aladejare, A.; Adediran, A.; Lawal, A.; Illikainen, M. Predicting shrinkage of alkali-activated blast furnace-fly ash mortars using artificial neural network (ANN). *Cem. Concr. Compos.* **2021**, *124*, 104265. [CrossRef]
35. Rachmatullah, M.I.C.; Santoso, J.; Surendro, K. Determining the number of hidden layer and hidden neuron of neural network for wind speed prediction. *PeerJ Comput. Sci.* **2021**, *7*, e724. [CrossRef] [PubMed]
36. Tran, H.N.; Nguyen, D.T.; Le, G.T.; Tomul, F.; Lima, E.C.; Woo, S.H.; Sarmah, A.K.; Nguyen, H.Q.; Nguyen, P.T.; Nguyen, D.D.; et al. Adsorption mechanism of hexavalent chromium onto layered double hydroxides-based adsorbents: A systematic in-depth review. *J. Hazard. Mater.* **2019**, *373*, 258–270. [CrossRef] [PubMed]
37. Colombo, A.; Geiker, M.; Justnes, H.; Lauten, R.; De Weerdt, K. The effect of calcium lignosulfonate on ettringite formation in cement paste. *Cem. Concr. Res.* **2018**, *107*, 188–205. [CrossRef]
38. Takahashi, H.; Ogawa, S.; Shibata, M.; Kuranaga, M.; Watanabe, S.; Mishiba, K.; Kawabata, Y. Expansion behavior of cement pastes containing additives due to delayed ettringite formation. In *Bridge Maintenance, Safety, Management, Life-Cycle Sustainability and Innovations*; Yokota, H., Frangopol, D.M., Eds.; CRC Press: Boca Raton, FL, USA, 2021; pp. 2659–2663. [CrossRef]
39. Bertos, M.F.; Simons, S.J.R.; Hills, C.D.; Carey, P.J. A review of accelerated carbonation technology in the treatment of cement-based materials and sequestration of CO_2. *J. Hazard. Mater.* **2004**, *112*, 193–205. [CrossRef]
40. Chang, J.; Xiong, C.; Zhang, Y.; Wang, D. Foaming characteristics and microstructure of aerated steel slag block prepared by accelerated carbonation. *Constr. Build. Mater.* **2019**, *209*, 222–233. [CrossRef]
41. Paul, K.T.; Satpathy, S.; Manna, I.; Chakraborty, K.; Nando, G. Preparation and Characterization of Nano structured Materials from Fly Ash: A Waste from Thermal Power Stations, by High Energy Ball Milling. *Nanoscale Res. Lett.* **2007**, *2*, 397–404. [CrossRef]
42. Patil, A.G.; Shanmugharaj, A.; Anandhan, S. Interparticle interactions and lacunarity of mechano-chemically activated fly ash. *Powder Technol.* **2015**, *272*, 241–249. [CrossRef]
43. Tian, X.; Rao, F.; León-Patiño, C.A.; Song, S. Effects of aluminum on the expansion and microstructure of alkali-activated MSWI fly ash-based pastes. *Chemosphere* **2020**, *240*, 124986. [CrossRef] [PubMed]
44. Siddique, S.; Jang, J.G. Acid and sulfate resistance of seawater based alkali activated fly ash: A sustainable and durable approach. *Constr. Build. Mater.* **2021**, *281*, 122601. [CrossRef]
45. Lodeiro, I.G.; Macphee, D.; Palomo, A.; Fernández-Jiménez, A. Effect of alkalis on fresh C–S–H gels. *FTIR analysis. Cem. Concr. Res.* **2009**, *39*, 147–153. [CrossRef]
46. Hong, S.-Y.; Glasser, F. Alkali binding in cement pastes: Part I. The C-S-H phase. *Cem. Concr. Res.* **1999**, *29*, 1893–1903. [CrossRef]

47. Li, N.; Farzadnia, N.; Shi, C. Microstructural changes in alkali-activated slag mortars induced by accelerated carbonation. *Cem. Concr. Res.* **2017**, *100*, 214–226. [CrossRef]
48. Thomas, S.; Meise-Gresch, K.; Müller-Warmuth, W.; Odler, I. MAS NMR Studies of Partially Carbonated Portland Cement and Tricalcium Silicate Pastes. *J. Am. Ceram. Soc.* **1993**, *76*, 1998–2004. [CrossRef]
49. Wang, X.; Ni, W.; Li, J.; Zhang, S.; Hitch, M.; Pascual, R. Carbonation of steel slag and gypsum for building materials and associated reaction mechanisms. *Cem. Concr. Res.* **2019**, *125*, 105893. [CrossRef]